



HAL
open science

Multi-sensor airborne lidar requires intercalibration for consistent estimation of light attenuation and plant area density

Grégoire Vincent, Philippe Verley, Benjamin Brede, Guillaume Delaitre, Elliott Maurent, James Ball, Ilona Clocher, Nicolas Barbier

► **To cite this version:**

Grégoire Vincent, Philippe Verley, Benjamin Brede, Guillaume Delaitre, Elliott Maurent, et al.. Multi-sensor airborne lidar requires intercalibration for consistent estimation of light attenuation and plant area density. *Remote Sensing of Environment*, 2023, 286, pp.113442. 10.1016/j.rse.2022.113442 . hal-03932451

HAL Id: hal-03932451

<https://hal.inrae.fr/hal-03932451v1>

Submitted on 8 Jan 2025

HAL is a multi-disciplinary open access archive for the deposit and dissemination of scientific research documents, whether they are published or not. The documents may come from teaching and research institutions in France or abroad, or from public or private research centers.

L'archive ouverte pluridisciplinaire **HAL**, est destinée au dépôt et à la diffusion de documents scientifiques de niveau recherche, publiés ou non, émanant des établissements d'enseignement et de recherche français ou étrangers, des laboratoires publics ou privés.



Distributed under a Creative Commons Attribution - NonCommercial 4.0 International License

1 Multi-sensor airborne lidar requires intercalibration for consistent
2 estimation of light attenuation and plant area density

3
4 Grégoire Vincent^{a*}, Philippe Verley^a, Benjamin Brede^{b,c}, Guillaume Delaitre^{a,e}, Elliott Maurent^{a,f},
5 James Ball^{a,g}, Ilona Clocher^{a,d}, Nicolas Barbier^a

6
7

8 Abstract

9 Leaf area is a key structural characteristic of forest canopies because of the role of leaves in
10 controlling many biological and physical processes occurring at the biosphere-atmosphere
11 transition. High pulse density Airborne Laser Scanning (ALS) holds promise to provide spatially
12 resolved and accurate estimates of plant area density (PAD) in forested landscapes, a key step in
13 understanding forest functioning: phenology, carbon uptake, transpiration, radiative balance etc.
14 Inconsistencies between different ALS sensors is a barrier to generating globally harmonised PAD
15 estimates. The basic assumption on which PAD estimation is based is that light attenuation is
16 proportional to vegetation area density. This study shows that the recorded extinction strongly
17 depends on target detectability which is influenced by laser characteristics (power, sensitivity,
18 wavelength). Three different airborne laser scanners were flown over a wet tropical forest at the
19 Paracou research station in French Guiana. Different sensors, flight heights and transmitted power
20 levels were compared. Light attenuation was retrieved with an open source ray-tracing code
21 (<http://amapvox.org>). Direct comparison revealed marked differences (up-to 25% difference in
22 profile-averaged light attenuation rate and 50% difference at particular heights) that could only be
23 explained by differences in scanner characteristics. We show how bias which may occur under
24 various acquisition conditions can generally be mitigated by a sensor intercalibration. Alignment of

25 light weight lidar attenuation profiles to ALS reference attenuation profiles is not always
26 satisfactory and we discuss what are the likely sources of discrepancies. Neglecting the
27 dependency of apparent light attenuation on scanner properties may lead to biases in estimated
28 vegetation density commensurate to those affecting light attenuation estimates. Applying
29 intercalibration procedures supports estimation of plant area density independent of acquisition
30 characteristics.

31

32 Introduction

33 Gas exchange processes between vegetation and the atmosphere are mediated by leaf surface. For
34 example, canopy temperature, energy balance, and photosynthetic rate are related to the amount
35 of leaf area (Bonan 2015) which is therefore a key variable in dynamic vegetation models.
36 Estimation of Leaf Area Index in evergreen forests has nonetheless remained a challenge and LAI is
37 still poorly resolved over space and time. This limits our ability to effectively
38 initialize/calibrate/validate or otherwise constrain vegetation models. Ground-based methods of
39 LAI measurements have well known limitations (Bréda 2003). Litterfall collection cannot provide
40 direct information without prior knowledge of the leaf lifespan which itself is highly variable within
41 site across species and environmental conditions (Osada et al. 2001; Reich et al. 2004; Laurans et
42 al. 2012). Indirect optical methods such as LAI2000 instrument or hemispherical photographs
43 essentially measure directional gap probability which allows to derive “effective LAI” rather than
44 actual LAI (Chen et al. 1997). Effective LAI is the expected LAI given the observed directional gap
45 probability under the assumption that light is intercepted only by leaves (no wood contribution)
46 and that foliage has a spatially random distribution (no clumping).

47 Extending the definition of Leaf Area Index proposed by (Chen and Black 1991), Plant Area Index
48 (PAI) can be defined as half the total plant area (considering all vegetation components including
49 branches and trunks) per unit horizontal ground surface area (Fang et al. 2019). Similarly, Plant
50 Area Density (PAD) is then half the total plant area per unit volume of canopy. In the present study
51 we are concerned with PAI and PAD only and will not address the problem of estimating the
52 contribution of woody elements to PAI.

53 Deriving PAI from Airborne Laser Scanning is an attractive alternative compared to other means of
54 estimation (Morsdorf et al. 2006; Hopkinson and Chasmer 2007; Solberg et al. 2009; Vincent et al.
55 2017; Almeida et al. 2019; Arnqvist et al. 2020). In contrast with direct ground measurements of
56 PAI which typically have a limited spatial coverage (Olivas et al. 2013), ALS can produce consistent
57 estimates over large areas capturing spatial variability of plant area density, leading to more
58 accurate spatially integrated estimates. Mapping PAI at landscape scale opens-up new
59 opportunities to study sources of variation of PAI, or to use such information as initial condition for
60 dynamic vegetation models (Longo et al. 2020). A key advantage of lidar over passive optical
61 methods is that it provides 3D-explicit information on light attenuation which allows to estimate
62 PAD per small unit volumes rather than for the entire canopy, thereby reducing the clumping bias
63 issue to the subunit volume scale (Vincent et al. 2017).

64 Direct estimate of LAI from passive optical remote sensing are based on the selective absorption of
65 solar radiation by green leaves in red and infrared bands. They tend to saturate at high LAI values
66 (Zheng and Moskal 2009). For instance the Normalized Difference Vegetation Index (NDVI)
67 saturates around LAI = 3.5 (Shabanov et al. 2005). Retrieval algorithms based on look-up tables
68 derived for typical canopy structures using stochastic radiative transfer equations are more

69 sensitive than direct correlative approaches. However uncertainty at high LAI remains high due to
70 the sensitivity of retrieval algorithm to the surface reflectance precision which is limited by
71 frequent cloud and aerosol contamination in the tropics (Fang et al. 2019). ALS derived estimates of
72 PAI may also saturate in tall dense vegetation. Dense vegetation may indeed favour high pulse
73 fragmentation rate with multiple returns of lower intensity. A significant fraction of the returns
74 may remain below the sensor's detection threshold, but this issue has received little attention so
75 far.

76 The recent increase in the number of surveys of individual sites that have multi-temporal lidar data
77 has however led to greater scrutiny of the consistency between acquisitions, notably in terms of
78 sensor induced systematic difference in PAI estimate. Shao et al. (2019) for instance have built on
79 the Sustainable Landscape Brazil data set and compared 4 sensors and 16 pairs of multitemporal
80 measurements. Each pair consisted of two lidar surveys conducted in different years. That study
81 showed that a statistical intercalibration between sensors using a single multiplicative factor
82 significantly improved consistency in PAI estimates obtained with different sensors.

83

84 Extending the analysis of Shao et al. (2019), in the present study we compare light extinction
85 profiles in a tropical forest canopy obtained with three different lidar sensors and under various
86 settings (different flight heights, or different transmitted power). The objectives were to evaluate
87 the level of sensitivity of light extinction profiles to acquisition conditions and also to identify the
88 sources of bias in order to better take them into account in multiple site or multiple date
89 vegetation surveys when identical acquisition settings are not granted.

90

91 The manuscript is organised as follows. The material and methods section briefly describes the
92 general modelling assumptions, the ray tracing software used to process the lidar data
93 (<http://amapvox.org>), the study site, the laser systems tested and the different flight plans operated.
94 Then the analysis is conducted in two steps. The first step consists in analysing, for the different
95 scanning scenarios, the level of completeness of retrieval of lidar backscattered energy and the
96 variability in lidar returns intensity. The objective of this first part is to determine a robust estimate
97 of the contribution of individual returns to the interception of an emitted laser pulse. The second
98 part explores the differences in light extinction profiles (proportional to PAD profiles) for the
99 different scanning scenarios. Those profiles are produced by using the return weighting scheme
100 determined in the first step. Different light extinction profile inter-calibration procedures are
101 tested. The discussion section examines both sets of results and further explores how an absolute
102 calibration might be achieved.

103

104 Material & Methods

105 Theoretical background

106 *PAD estimation from ALS data*

107 Most methods proposed for estimating PAI from airborne lidar data build on the fundamental
108 dependency between plant area density and light extinction rate. The theory describing light
109 attenuation through canopies has a long history (e.g. (Miller 1967; Ross 1981)) and has served as
110 the basis for describing lidar pulse extinction in forest canopies.

111 The Beer-Lambert law is commonly used to describe light extinction through a canopy layer.

$$\frac{I_l}{I_0} = \exp(-\lambda l)$$

Equation 1

112 Where I_0 is the incoming light intensity, I_l is the remaining light intensity after travelling a distance
113 l through the canopy and λ is the attenuation coefficient. This attenuation coefficient is
114 proportional to the Plant Area Density ($\text{m}^2\cdot\text{m}^{-3}$) and is also affected by other vegetation
115 characteristics such as clumping and orientation of scatterers which may further introduce a
116 dependency of attenuation on light incidence angle (Bréda 2003).

117

118 ALS derived canopy transmittance is obtained from the analysis of the return pulse waves of light
119 reflected by the targets. Multiple hits occur if successive targets only partially intercept the source
120 light pulse. If the targets are sufficiently large and sufficiently distant from each other, then distinct
121 returns can be recorded. For each emitted pulse, some systems record all detectable returns (e.g.
122 Riegl LMSQ 780, Riegl VUX-1UAV this study). Other systems are limited to a fixed maximum
123 number of returns (e.g. five returns for the Riegl miniVUX, this study). Lidar systems typically
124 record the strength of the backscattered echoes (often the peak power). However, a proper
125 radiometric calibration is required to gain access to the echo energy (Wagner 2010).

126

127 In a detailed simulation study, Yin et al. (2020) examined the performance of various descriptors
128 extracted from ALS data which had previously been used to estimate canopy transmittance and
129 PAI. The metrics considered were derived from a ratio of traversing pulses over entering pulses.
130 They differed however in the choice of the return numbers used for calculation (first, last, both, all)
131 and whether these were weighted or not, and in the former case how they were weighted: by the
132 inverse of the echo number per shot or by the recorded return intensity. They concluded that
133 methods using return intensity for weighting the echoes were more accurate overall and less

134 influenced by variations in footprint size, leaf area, vegetation cover, and foliar dimensions than
135 the methods based on return counts only. Unfortunately, even when the individual echo energy is
136 retrievable from the recorded signal, the physically based approach advocated by the authors may
137 not be generally applicable. Indeed, the heterogeneity of a forest canopy and the high variability in
138 optical properties of natural surfaces which affect the amount of light reflected towards the sensor
139 may largely obscure the link between the target projected area and the returned energy (see
140 below).

141 The lidar signal may also vary with atmospheric characteristics. If atmospheric conditions are known, the
142 attenuation of lidar signal can be estimated from atmospheric transfer simulations (Wagner 2010).
143 Alternatively, flight campaign calibration using targets of known optical properties can be attempted.
144 Atmospheric extinction generally results both from scattering and absorption. Effect of
145 atmospheric water content in the infra-red range was examined for laser ranger finders operating
146 at 905 nm and 1550nm (Wojtanowski et al. 2014). That study reported a low impact of
147 atmospheric humidity on extinction coefficients at both wavelengths. Fog however significantly
148 decreased the detection range at both wavelengths and more so at 1550nm.

149 Surface wetness may also affect lidar return signal strength significantly. Kaasalainen et al. (2009) reported a
150 decrease in reflectance of a series of targets (sand, brick, concrete) of 30-50% between dry and wet surfac-
151 es. WeiChen et al. (2015) operating a Leica ALS60 under different acquisition configurations reported a pen-
152 etration rate (defined as the proportion of pulses generating a ground return to the total number of emitted
153 laser pulses) reduced by approximately 25% in case of wet ground. This was attributed to the low reflec-
154 tance of water in the near infrared range beyond 800 nm.

155

156 *Lidar back-scattering model*

157 For a target with Lambertian surface, larger than the foot print size and of solid angle π steradians
158 the following relation between the received Power P_r to the transmitted power P_t has been
159 proposed (Höfle and Pfeifer 2007)

160

$$P_r = \frac{P_t D_r^2 \rho}{4R^2} \eta_{sys} \eta_{atm} \cos \alpha \quad \text{Equation 2}$$

162

163 Where R is the distance from sensor to target, α is the incidence angle, η_{sys} and η_{atm} are system
164 and atmospheric transmission factors respectively, D_r is the receiver aperture diameter, and ρ is
165 the target reflectance.

166 η_{sys} , D_r are considered constant for a given flight campaign and variation in η_{atm} between flight
167 lines may be neglected in first approximation. Variation in η_{atm} is implicitly neglected between
168 flight campaigns.

169

170 Critically, when using lidar one derives transmittance (or attenuation) from a measurement of
171 reflected, not transmitted light. An implicit assumption is that all the hits will generate a return
172 wave detectable by the sensor or, at least, that undetectable targets are sufficiently few to be
173 ignored without significantly biasing transmittance estimation. However, this may not hold true at
174 all times. Vegetation is typically composed of many scatterers, irregular in their spatial distribution,
175 size, orientation and shape. Small or poorly reflective targets may not backscatter enough energy
176 towards the sensor for a return to be detected. A fraction of the laser pulses may also be deflected
177 away from sensor due to specular reflection as it is commonly observed over water bodies.

178 The energy associated with each return will depend on the fraction of the pulse which is
179 intercepted as well as on the reflectivity and orientation of the intercepting surface (Höfle and
180 Pfeifer 2007; Yin et al. 2020). Natural surfaces, however, tend to have highly variable optical
181 properties (across material e.g. wood versus leaves, between ground and vegetation, depending
182 on surface wetness, etc) which limits our ability to precisely characterise those properties.

183

184 *Light attenuation profile computation*

185 AMAPVox (<http://AMAPVox.org>) is an open source software designed to analyze lidar-vegetation
186 interactions. It can process various discrete lidar data type: single or multiple returns, terrestrial or
187 airborne.

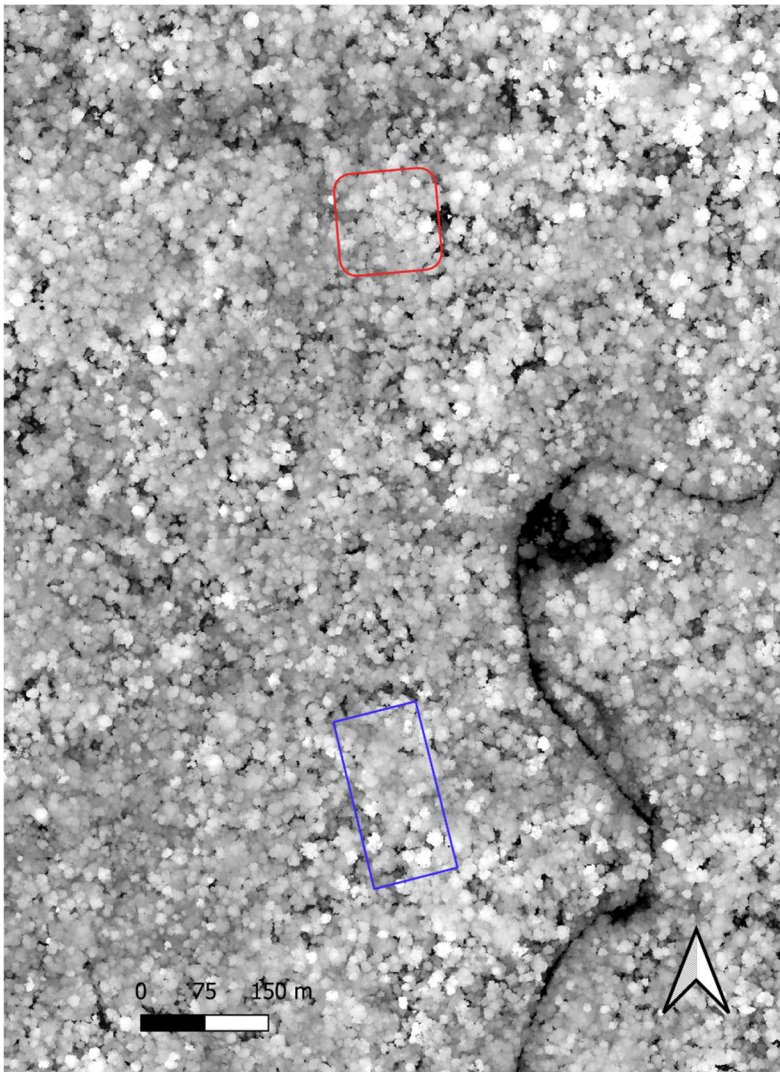
188 AMAPvox tracks every laser pulse through a 3D grid (voxelized space) from the laser head to the
189 last recorded hit. The effective sampling area of each laser pulse (or fraction of pulse in case of
190 multiple hits) is computed from the theoretical beam section (a function of distance from laser and
191 divergence of laser beam) and the remaining beam fraction entering a voxel. Different weighting
192 options of individual returns are available which may include the individual return intensity. This
193 information is combined with the optical path length of each pulse entering a voxel to compute the
194 local attenuation per voxel. Different estimation procedures are provided in the AMAPVox
195 software (Vincent et al. 2021). In the present study we used the maximum likelihood estimate of
196 the attenuation coefficient coined “Potential Path Length” in AMAPvox (Vincent et al. 2021). This
197 3D description of local attenuation can then be horizontally integrated under consideration of the
198 ground elevation to compute canopy attenuation profiles.

199

200 Study location

201 The lidar overflights were conducted over the experimental site of Paracou in French Guiana (see
202 location map in (Vincent et al. 2012)) during the annual long dry season (September-November) in
203 2016, 2019 and 2020. The mean canopy height of the forest at Paracou is c. 27.8 m (standard
204 deviation = 3.0) and the mean basal area c. 30m²/ha in the unlogged plots (Vincent et al. 2010;
205 Vincent et al. 2012). Two regions of interest were arbitrarily selected (a 1.4-ha plot and a 2-ha plot)
206 that are covered with undisturbed old growth tropical moist forest (Figure 1).

207



208

Figure 1: Paracou canopy height model (2019) with outline of ROI1 (red) and ROI2 (blue)

209 Lidar Systems

210 The *RIEGL* miniVUX-1UAV (905 nm) is a lightweight UAV-borne laser scanner, designed specifically
211 for integration with UAV (Table 1). It uses online waveform processing, multi-target resolution (up-
212 to 5 target echoes per laser shot). Beam divergence (measured at 50% peak intensity) is less than
213 1.6 x 0.5 mrad (*RIEGL Laser Measurement Systems* 2020). The long axis of the resulting elongated
214 footprint is 16 cm and the short axis 5cm at 100m distance with a resulting footprint area of 0.008
215 m².

216

217 The *RIEGL* VUX-1UAV (1550nm) is about twice as powerful (Table 1) and heavy as the miniVUX. The
218 Pulse Repetition Rate (PRR) of the VUX is adjustable from 50kHz to 550kHz. As the product of PRR
219 and pulse power is constant changing PRR also affects pulse power (*RIEGL Laser Measurement*
220 *Systems* 2020). The divergence is less than 0.5 mrad ($1/e^2$). The foot print diameter is 5 cm at
221 100m distance (0.002 m²).

222

223 The *RIEGL* LMS-Q780 (1064 nm) is designed to be carried onboard a manned aircraft. It is a digital
224 full waveform sensor that provides access to detailed target characteristics by digitizing the echo
225 signal online during data acquisition and also allowing subsequent full waveform analysis. Beam
226 divergence (measured at the $1/e^2$ point) is less than 0.25 mrad (*RIEGL Laser Measurement Systems*
227 2015). The footprint diameter is 22.5 cm at 900m distance (area of 0.04 m²) and 11.25 cm at 450m
228 (area of 0.01 m²).

229

230 Beam divergence increases from 0.25 mrad (LMS-Q780) estimated at 0.135 peak power to 1.6*0.5
 231 mrad (minivux) estimated at 50% of peak power. The footprint shape of the miniVUX is not circu-
 232 lar and the divergence is given in two orthogonal directions. The difference in divergence is large
 233 and not easy to properly quantify given the different definition used for the miniVUX and the oth-
 234 er two sensors. Importantly increased beam divergence means more rapid decrease in target irra-
 235 diance (i.e. radiant flux received per unit area) which varies as the inverse of footprint area.

Table 1: Lidar sensor characteristics

Characteristic	LMSQ780	VUX-1UAV	miniVux -1 UAV	Comments
Weight	20 kg	3.65kg	1.6kg	-
Laser wavelength	1064 nm	1550 nm	905 nm	-
Beam divergence (mrad)	<=0.25	<=0.5	<=1.6*0.5	Different definition of divergence used for miniVux
Footprint diameter	22.5 cm @ 900m	5cm @ 100m	16*5 cm @ 100m	Non-spherical foot print of miniVUX
Pulse duration and range resolution	4.5 ns (0.75 m)	3 ns (0.45 m)	6 ns (0.9 m)	range resolution is defined as (group velocity * pulse duration) /2 (Wagner et al. 2006)
Adjustable power	Yes	Yes	No	
Maximum range (natural target of reflectivity > 60%)	2400m @25% power	660m @100% power	290m @100% Power	Assuming 23 km visibility, flat target in excess of foot print size, orthogonal to laser beam
Maximum number of recorded returns per pulse	Unlimited (observed 7)	Unlimited (observed 9)	5 (observed 5)	

236
 237 We used the extra-byte information provided by RIEGL instruments (Riegl Laser Measurement
 238 Systems 2019) to normalize the return intensity with regard to distance as explained in the next
 239 paragraph.

240 All three instruments record the signal amplitude which is the optical input power relative to the
 241 instrument detection threshold (in dB).

242 For the miniVUX-1UAV and the VUX the normalized intensity was simply taken as the target
243 relative reflectance value, i.e. the ratio of the actual echo amplitude to the amplitude of a white
244 flat target at the same range, orientated orthonormal to the beam axis, and with a size in excess of
245 the laser footprint. This was expressed as a fraction (between 0 and 1) rather than in dB, so that
246 reflectance of successive echoes generated from a single emitted pulse could be meaningfully
247 summed.

248 For the LMSQ780, normalized intensity was taken as (Vincent et al. 2017)

249
250
$$I = 10^{A/10} * d^2 * W * K$$
 equation 3

251
252 Where A (amplitude) is the optical power in dB, d (range) is the distance from source to target in
253 m, W (pulse width) is defined as full width at half maximum of the received echo signal and is
254 measured in nanoseconds (ns), and K is an arbitrary constant.

255 In the rest of the manuscript, intensity refers to the above-mentioned normalized intensities which
256 are corrected for target range dependency. Note that while intensity values can be meaningfully
257 compared for VUX and miniVUX data, the LMSQ780 values are provided on a different scale.

258
259 Flight plans

260 Two different tracts of undisturbed forest outlined on Figure 1 served to compare sensors,
261 hereafter referred to as ROI1 (1.4ha) and ROI2 (2ha).

262

263 **ROI1 flight plans**

264 On this area we compared the LMSQ780 (different transmitted power and different flight heights)
265 with the miniVUX-1UAV (operated at different flight heights). Scanning angles of all flights were
266 limited to +/- 15 degrees off nadir to control for possible anisotropy in light extinction.

267

268 We considered two different campaigns operating the LMSQ780 over the same region of interest.

269 Those campaigns took place in October 2016 and November 2019, both during the dry season.

270 Due to variation in flight altitude and number of contributing flight lines (Table 2 and Table 3) the

271 final pulse density varied across the different flight configurations from 9 to 22 pls. m⁻².

272 Pulse density achieved with the miniVUX-1UAV (MNVX) was an order of magnitude higher,

273 between 175 and 186 pls. m⁻² (Table 3).

274

275 List of flights over ROI 1

276 • LMSQ780 (ALS) 19 September 2016, 3 flight heights (430m, 630m and 830m) and 2
277 transmitted power (6% and 12% full power)

278 • LMSQ780 (ALS) 15 November 2019, single flight height (900m), 25% full power

279 • MNVX (UAV-LS) 19-20 October 2020, 3 flight heights

280

281 **ROI2 flight plans**

282 Over the second ROI all data were acquired the same year during the dry season. Scanning angles

283 of all flights were also limited to +/- 15 degrees off nadir.

284 List of flights over ROI 2

285 • LMSQ780 (ALS) 15 November 2019 single flight height, 25% full power, pulse density 19
286 pls.m⁻².

- 287 • MNVX (UAV-LS) 18 October 2019 single flight height, pulse density 85 pls.m⁻².
288 • VUX (UAV-LS) 10-21 October 2019 single flight height, 3 power levels (100%, 33%, 18%) and
289 pulse densities (64, 187 and 369 pls.m⁻²).

290

291 Lidar data processing and data analysis

292 The complete LMSQ780 2019 data set was used to produce a Digital Terrain Model. The
293 consolidated pulse density was 40 pls.m⁻² for a scanning swath angle of +/- 30 degrees. Ground
294 point filtering procedure is described in Appendix 1. All returns less than 50cm above the modelled
295 ground surface were considered ground points to compute the three following indicators: ground
296 point density (pt.m⁻²), fraction of transmitted pulses reaching the ground (%), and proportion of
297 energy reaching the ground. In the latter case, ground returns were weighted by the inverse of
298 their return rank.

299

300 In the first part, we analyse the overall statistics per flight to firmly establish that target detection
301 rate varies with at-canopy-irradiance (radiant power received per unit area of surface) for all three
302 sensors.

303 Focusing on single (i.e. potentially unfragmented) returns we then investigate how reflectance
304 varies across space. We illustrate the variability in reflectance across individual crowns by mapping
305 single return intensity for the three sensors (ROI2). We further examine the dependency of single
306 return intensity to canopy depth and height above the ground for the different sensors using
307 multiple linear models. We also examine how individual return intensity varies with return rank.
308 These pieces of information are combined to determine the individual return contribution to light
309 interception used when computing light extinction with AMAPVox (part 2).

310

311 In the second part we move on to compare light extinction profiles for the different flights. The
312 LMSQ780 2019 data were considered as the reference data when intercalibrating profiles as this
313 campaign covered both ROIs.

314 Lidar data were voxelized at 2x2x2 m resolution. This resolution ensured that at least 90% of the
315 lower most voxels were sampled by the reference lidar campaign (Appendix 2). A mean
316 attenuation profile was computed for each flight over the areas of interest. Sensitivity of
317 attenuation profiles to pulse density was found to be low. For instance, a 50% thinning of lidar
318 pulses applied to the reference flight (density reduced to 10 emitted pulses per m², c. 20 return
319 pulses) generated a relative Root Mean Square Error (RMSE) of less than 2% in the attenuation
320 profile values. This was in line with previous observations reporting stable LAD profiles (at ¼ ha
321 resolution) above 20 return pulses per m² (Shao et al. 2019).

322

323 The calibration procedure involved fitting the targeted attenuation profile to the reference profile.
324 This was achieved by linear regression using R software (R Core Team. 2022) . Calibration functions
325 were adjusted at the level of the vegetation profile rather than the individual voxel level. Indeed,
326 given the uncertainty of individual voxel estimations (which acted as the predictors in the
327 regression as well as the response variable) the regressions would have been biased (Frost and
328 Thompson 2000). This uncertainty at voxel scale was systematically higher for lower vegetation
329 layers due to the lower sampling intensity consecutive to the attenuation of the lidar signal
330 travelling down the canopy. This uncertainty was further amplified by the time difference between
331 some of the campaigns which were compared (e.g. LMSQ780-2019 vs MNVX-2020 or LMSQ780-
332 2019 vs LMSQ780-2016).

333 Simple linear regressions without intercept were always considered first (corresponding to a single
334 calibration coefficient). Additional predictors such as mean distance to laser or mean canopy depth
335 (i.e. distance from top of canopy) were also tested to try to improve the fit.

336 Results

337 Global statistics per flight

338 During the ALS campaign conducted in 2016 various flight heights and laser power settings were
339 compared. Reducing transmitted power (compare column 2 and 3, in Table 2) led to a decrease in
340 mean number of returns per pulse, and a decrease in the cumulated fraction of pulses reaching
341 the ground. Reducing flight height (compare column 1 to 2 in Table 2) led to an increase in mean
342 return number per pulse, an increase in the proportion of pulses triggering a ground return and an
343 increase in the cumulative fraction of pulses reaching the ground.

344 MiniVUX (Table 3) and VUX (Table 4) had lower penetration than LMSQ780 as measured by the
345 lower fraction of pulses reaching the ground and the lower cumulated fraction of pulses reaching
346 ground. MiniVUX and VUX also had fewer returns per pulse and fewer pulses generating more than
347 one return. The miniVUX and VUX sensors showed trends in relation to change in canopy
348 irradiance similar to the LMSQ780 both in terms of number of returns per pulse and penetration.

349

Table 2: **ROI 1** (1.4 ha) statistics computed for 2016 ALS flights (2016) –

LMSQ780 - flight height	High	Low	Low
Power setting	12%	12%	6%
Number of Flight lines	4	1	2
Median Height above ground in m + [min;max]	835 [802;849]	422 [421;425]	427 [424;436]
Average Foot print size at ground level (cm ²)	342	87	90
Reflectance detection threshold at ground level Beam orthogonal to target, no fragmentation, clear sky*	11%	<5%	5%
Mean scan angle from vertical (deg) + [min;max]	-2.14 [-7;+2]	-0.05 [-13;+13]	-3.83 [-13;+5]
Pulse density (pls.m ⁻²)	19	9	17
Ground point density ** (pt.m ⁻²)	0.89	0.70	0.97
Shots reaching ground **	4.8 %	7.6 %	5.7%
Cumulated fraction of returns reaching ground ***	1.6 %	2.1%	1.7%
Mean Number Of Returns per pulse	1.95	2.23	2.05
Fraction of Single Returns	0.36	0.29	0.34

* (RIEGL Laser Measurement Systems 2022)

** all returns up to 50cm above the modelled ground surface included

*** assuming balanced fragmentation

350
351
352
353
354

Table 3: **ROI 1** (1.4 ha) statistics computed for DLS (2020) and LMSQ780 (2019) flights-

	LMSQ780	MNVX Lowest height	MNVX Medium height	MNVX Highest
Flight code		195113	110932	201241
Power setting	25%	100%	100%	100%
Median Height above ground in m + [min;max]	891 [865;937]	58 [56;61]	71 [68;74]	104 [101;108]
Reflectance detection threshold at ground level Beam orthogonal to target, no fragmentation, clear sky*	7%	<5%	<5%	8%
Average Foot print size at ground level (cm ²)	360	27	40	87
Mean scan angle from vertical (degrees)	+0.36	+0.16	+0.05	-0.02
Pulse density **	22 (40)	160 (557)	175 (678)	173 (602)
Ground point density *** (pt.m ⁻²)	1.21	3.95	3.63	3.21
Shots reaching ground ***	5.4%	2.5%	2.1%	1.9%
Cumulated fraction of returns reaching ground ****	2.1 %	1.1%	1.0%	0.9%
Mean number of return per pulse	2.2	1.45	1.42	1.40
Fraction of single returns	0.28	0.64	0.66	0.66

* (RIEGL Laser Measurement Systems 2022)

355
356

357 **+/-15 degrees (full density in brackets)
 358 *** all returns up to 50cm above the modelled ground surface included
 359 **** assuming balanced fragmentation
 360

Table 4 : **ROI 2** (2 ha) statistics computed for 2019 ALS, MNVX and VUX flights-

	LMSQ780	MNVX	VUX 100kHz	VUX 330kHz	VUX 550kHz
Power setting	25%	100%	100%	33%	18%
Median Height above ground in m + [min;max]	904 [878;927]	82 [78;85]	118 [105;129]	117 [105;127]	117 [106;127]
Reflectance detection threshold at ground level ; Beam orthogonal to target, no fragmentation, clear sky*	7%	<5%	<5%	5%	9%
Estimated Foot print size at ground level (cm2)	401	54	27	27	27
Mean scan angle	1.08	1.24	0.59	0.62	0.65
Pulse density **	19 (34)	82 (218)	65 (141)	187 (408)	369 (792)
Ground point density*** (pt.m ⁻²)	0.97	0.71	2.58	5.70	8.82
Shots reaching ground****	5.2%	0.9%	4.0%	3.0%	2.4%
Cumulated fraction of pulses reaching ground****	2.0 %	0.4%	1.4%	1.2%	1.1%
Mean number of returns per pulse	2.2	1.4	1.8	1.7	1.6
Fraction of single returns	0.29	0.66	0.47	0.49	0.53

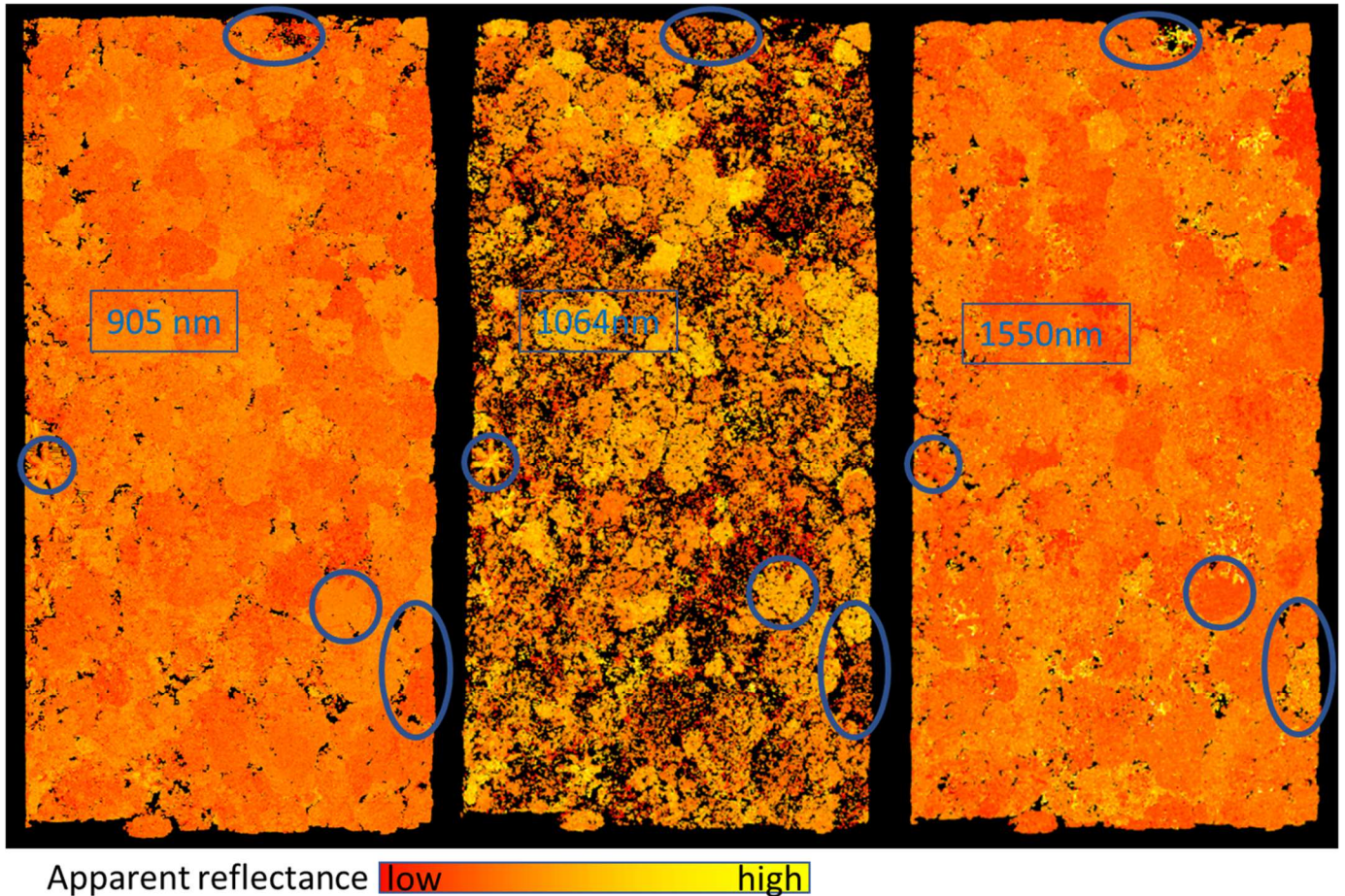
361 * (RIEGL Laser Measurement Systems 2022)
 362 **+/-15 degrees scan angle (full density in brackets)
 363 ***all returns up to 50cm above the modelled ground surface included
 364 **** assuming balanced fragmentation
 365

366 Variability in backscattered energy

367 *Single returns intensity varies across crowns*

368 We selected single returns classified as vegetation in 3 sample datasets over ROI2 (LMSQ780 25%
 369 power, VUX full power, miniVUX) to map the canopy reflectance (Figure 2). Single return intensity
 370 was clearly structured per crown. It was also noticeable that ranking of individual crown
 371 reflectance was not consistent across sensors.

372 On Figure 2- right panel the high intensity returns which appear in yellow can distinctively be traced
373 to branches and trunks by examining the point cloud. Wood reflectivity is indeed typically higher
374 than leaf reflectivity at 1550 nm (Brede et al. 2022).
375



376

Figure 2: Intensity of single returns (ROI 2) by three sensors of different wavelength illustrating crown to crown variation. Left miniVUX 905nm, center ALS 1064nm, right VUX (scan angle restricted to +/-15 degrees) - Different absolute scales are used for different sensors; Some crowns are highlighted to illustrate the fact that intensity ranking is not preserved across laser wavelengths

377 *Single return intensity varies with canopy depth*

378 We examined whether a systematic change in reflectivity along the vertical canopy profile would
379 occur as a consequence of a change in vegetation characteristics (leaf/wood ratio or leaf water
380 content for instance). Because position in canopy and return rank were highly correlated due to
381 the overhanging scanning position, we restricted the analysis to single returns for all flights,
382 excluding ground points. We normalized individual return intensity by dividing by the mean return
383 intensity for each flight. We then fitted a linear model with a fixed intercept equal to one (the
384 overall mean intensity), with height above ground (HAG) and distance from top of canopy (DTC) as
385 continuous predictors (no interaction term). Albeit both predictors were correlated (typically
386 $r \sim 0.75$) dropping one of the predictors often significantly reduced the goodness of fit (Table 5).

387

388 While the proportion of total variance in single return intensity attributable to position in canopy
389 (HAG + DTC) was always low to very low (Table 5) it was also statistically highly significant. When
390 considered individually, DTC usually made a larger contribution than HAG to r^2 (Table 5, last two
391 columns). Recorded intensity by the VUX (1550nm) showed the largest variation with canopy
392 depth.

393

394 Table 5 : R^2 of linear prediction model of single return intensity as a function of HAG, DTC or both (Full); HAG: Height
395 Above Ground, DTC: Distance to Top of Canopy; All models have F statistic with p value < 0.001). The coefficients of
396 both predictors for the full model are also reported (HAG eff. And DTC eff.)

ROI	Sensor	Flight	Full model	HAG eff.	DTC eff.	HAG	DTC
1	miniVUX	58m AGL	0.024	-7.5E-03	-1.1E-03	0.004	0.011
1	miniVUX	71m AGL	0.003	-1.7E-03	-4.2E-04	0.001	0.000
1	miniVUX	104m AGL	0.021	-5.8E-03	-7.8E-04	0.002	0.011
1	LMSQ780	430m AGL 12% power	0.010	7.7E-03	2.3E-04	0.000	0.010
1	LMSQ780	430m AGL 6% power	0.002	2.8E-03	3.5E-05	0.000	0.002
1	LMSQ780	830m AGL 12% power	0.006	5.5E-03	5.1E-05	0.000	0.006
1	LMSQ780	900m AGL 25% power	0.001	-5.9E-04	-2.7E-04	0.001	0.000

2	VUX	100kHz-100% power	0.025	-1.0E-02	-1.1E-03	0.002	0.017
2	VUX	330kHz-33% power	0.041	-1.2E-02	-1.3E-03	0.002	0.028
2	VUX	550kHz-18% power	0.044	-1.1E-02	-1.3E-03	0.002	0.030
2	LMSQ780	900m AGL, 25% power	0.002	3.5E-03	1.3E-04	0.000	0.002
2	miniVUX	82m AGL	0.002	-1.7E-03	-3.2E-04	0.001	0.001

398

399

400 For each flight we then corrected the complete data for HAG and DTC estimated effects by
 401 applying the same multiplicative correction factor (function of HAG and DTC) which was estimated
 402 for single returns, to the entire set of vegetation returns. On this corrected data set we analyzed
 403 how the cumulated intensity per emitted pulse would vary with the number of returns per pulse.
 404 We also conducted this analysis on the uncorrected data set for comparative purposes (Figure 3).

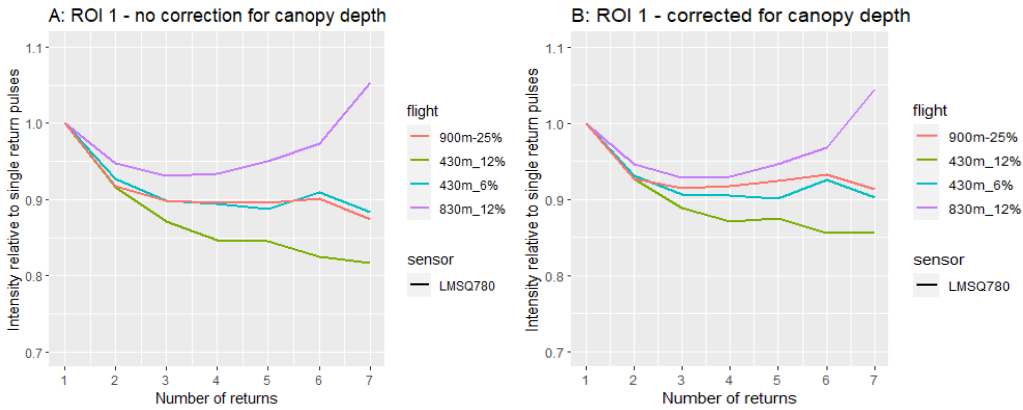
405 As a result of this correction, the initially observed trend for the VUX of mean cumulative return intensity to
 406 increase with pulse fragmentation almost disappeared (Figure 3F). This correction affected less the energy
 407 conservation patterns of the other sensors. It increased slightly the apparent loss with fragmentation
 408 observed for the miniVUX.

409

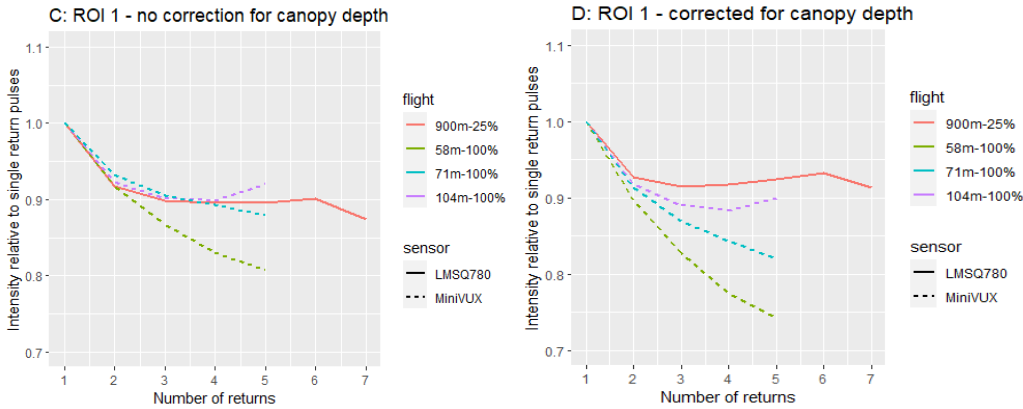
410 The mean cumulated intensity per shot varied with the level of pulse fragmentation (Figure 3). A
 411 decrease in mean return energy was noticeable from single to multiple return shots for LMSQ780
 412 and miniVUX (both plots). This decrease in cumulated intensity was more pronounced for lower
 413 flight heights (at a given laser power) or for higher laser power (at a given flight height) see Figure
 414 3A.

415

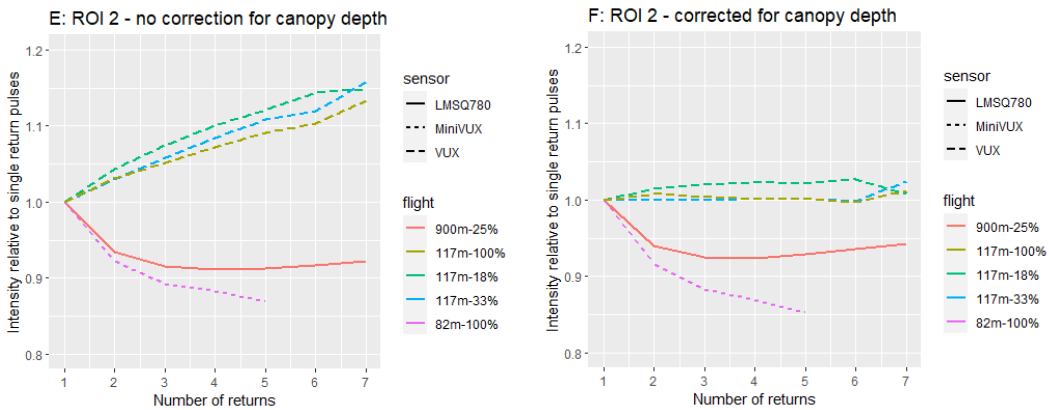
416



417



418



419

Figure 3 Mean cumulative intensity per shot (intensity) as a function of the number of detected returns (Number of returns); only shots not triggering a ground echo are considered. First line (A & B) considers different scanning settings for the same sensor. Second line (C & D) shows response for two different sensors. Third line (E & F) compares three different sensors. A, C & E (left): no intensity correction for canopy depth. B, D & F (right): systematic change in intensity occurring with canopy depth was corrected prior to analysis (see text).

420 The uncorrected VUX data showed an increase in cumulated intensity with degree of
421 fragmentation (Figure 3E). After correcting for systematic variation of intensity with canopy depth
422 this trend was barely discernible (Figure 3F). The strong dependence of return intensity on canopy
423 depth, which was probably not completely compensated for, make this data set difficult to
424 interpret in terms of patterns of backscattered energy retrieval. However, it can be noted that
425 increasing the VUX power from 18% to 100% increased the mean vegetation single return intensity
426 by 17% (from 0.24 to 0.29, Table 6), indicating that a fraction of the single returns were incomplete
427 returns, at least when power was less than 100%.

428

429 Somewhat unexpectedly, decreasing the miniVUX flight height (and thereby increasing irradiance
430 and detection rate) did not lead to a systematic increase in mean vegetation single return intensity
431 (instead a less than 4% and non-monotonous change was observed across flights; intensity of
432 single returns was 0.33, 0.32 and 0.34 for 58 m, 71 m and 104 m height of flights, ROI1-CNES).
433 However, the decrease in cumulated return intensity with fragmentation was more pronounced at
434 higher at-canopy irradiance (Figure 3C and 3D, dotted lines). This is consistent with an increased
435 proportion of “incomplete returns” and a lower detection rate (lower number of returns) with
436 decreased irradiance (Table 3) for higher flights.

437

438 In the case of the LSMQ780, it was observed that, like for the miniVUX (ROI1), higher at-canopy-
439 irradiance was associated with a stronger decrease in cumulated intensity following fragmentation
440 (compare for instance 900m_25% and 830m_12% or 430m_12% and 430m_6%, in Figure 3A or 2B).
441 It was also found, like for the VUX (ROI2), that higher irradiance determined a higher mean

442 vegetation single return intensity. For instance, single return intensity at 12% power was 649 and
 443 702 (arbitrary units) for 830 and 430m flight height, i.e. an 8% increase followed from at-canopy-
 444 irradiance being multiplied by 4 (as footprint area was divided by 4).

445

446 The cumulated retrieved energy per shot appeared to plateau (or even to increase, see for ex.
 447 830m_12% flight in Figure 3A or 3B) as the number of returns increased for the lowest at-canopy-
 448 irradiance values.

449

450 In addition, the mean vegetation to ground intensity ratio varied with wavelength as reported for
 451 ROI2 in Table 6. Values higher than one indicate a higher reflectivity of ground which may
 452 negatively bias the estimation of light extinction by vegetation. Indeed, if the compact background
 453 is more reflective than the porous medium in the foreground then it will be detected more
 454 effectively than potential targets in the foreground and transmittance may be overestimated.
 455 Conversely values lower than one may positively bias estimates of attenuation by vegetation.
 456 Those effects will affect detection rate more significantly under lower irradiance.

457 Mean single return ground intensity was larger than mean vegetation single return intensity for the
 458 VUX, and the ratio increased with at-canopy-radiance. So did the mean single return intensity as
 459 more partial hits were detected.

Table 6: Mean intensity of ground and vegetation single returns (ROI 2); standard deviation given in parenthesis

Sensor	Flight spec.	Ground	Vegetation	Ratio
VUX	100kHz - 100% power	0.415 (0.155)	0.286 (0.092)	1.45
VUX	330kHz - 33% power	0.375 (0.127)	0.262 (0.078)	1.43
VUX	550kHz - 18% power	0.320 (0.095)	0.239 (0.068)	1.34
LMSQ780	25% power – 900m AGL	211 (119)	209 (62)	1.01
miniVUX	82m AGL	0.303 (0.085)	0.334 (0.077)	0.90

460

461 We computed the intensity per rank (per number of return) for all flights over each ROI (*Table 7*)
462 excluding all shots reaching the ground. The common general pattern was for intensity per return
463 pulse to decrease with successive hits as the pulse effective footprint size (i.e. remaining foot print
464 size after partial interception) was gradually reduced. As the number of returns increases above 4
465 or 5, a conditional sampling effect tended to compensate for this, since likelihood of detecting
466 more targets is reduced if foremost targets are larger.

467

468 The weighting of individual return which was finally used for computing the attenuation profiles
469 (next section) is depicted in Table 7 below. It was derived from data collected using LMSQ780 at
470 25% power over ROI 2. Note that for number of returns larger than 7 data from VUX at 100%
471 power were used instead since no pulses with more than 7 returns were recorded using the
472 LMSQ780 (Table 1).

473

474 *Table 7: Mean relative intensity per return (corrected for systematic variation with canopy depth and height above*
475 *ground)- ROI2 LMSQ780-25% complemented with VUX 100kHz for number of returns >7; relative standard error (%) of*
476 *mean intensity in parenthesis. Excluding all shots reaching the ground.*

Return rank Number of returns	1	2	3	4	5	6	7	8	9
1	1.00 (0.04)	-	-	-	-	-	-	-	-
2	0.66 (0.06)	0.34 (0.10)	-	-	-	-	-	-	-
3	0.45 (0.09)	0.35 (0.10)	0.20 (0.13)	-	-	-	-	-	-
4	0.33 (0.17)	0.30 (0.16)	0.22 (0.18)	0.15 (0.20)	-	-	-	-	-
5	0.25 (0.37)	0.24 (0.35)	0.21 (0.36)	0.17 (0.38)	0.13 (0.39)	-	-	-	-
6	0.19 (1.01)	0.21 (0.94)	0.18 (0.94)	0.17 (0.98)	0.14 (0.97)	0.11 (0.98)	-	-	-
7	0.15 (3.29)	0.17 (2.94)	0.16 (3.17)	0.16 (3.28)	0.14 (3.38)	0.12 (3.30)	0.10 (3.18)	-	-
8	0.11 (13.20)	0.19 (10.18)	0.23 (12.71)	0.08 (18.80)	0.09 (15.12)	0.15 (12.47)	0.08 (12.75)	0.07 (15.22)	-
9	0.28 (10.86)	0.18 (70.55)	0.05 (40.13)	0.05 (57.98)	0.22 (87.69)	0.14 (10.79)	0.03 (71.11)	0.02 (96.60)	0.03 (3.01)

477

478 By considering a single matrix of weights for all flights we assumed those weights to be valid across
479 scanning scenarios. The actual pattern of pulse fragmentation is not expected to depend on the
480 wavelength or the transmitted power. However, differences in detection rate across scanning
481 scenarios will inevitably affect the relative intensity per return and therefore the mean weight per
482 return. The matrix used is therefore necessarily approximate.

483 We also considered the option consisting in adjusting a matrix of weights derived from each flight
484 data (with or without prior correction of intensity variation with canopy depth). Doing so did not
485 systematically or significantly reduce discrepancy between raw profiles or corrected profiles (i.e.
486 profiles obtained after applying a calibration function, see next section).

487

488 Concurrently to the decrease in return intensity with increasing return rank (Table 7), we observed
489 (Figure 3 A, B, C, D) that higher fragmentation (higher number of returns per emitted pulse) was
490 associated with a lower cumulative intensity.

491

492 Intercalibration of ALS flights

493 Can ALS flights be intercalibrated in such a way that overflights conducted under different
494 acquisition settings at different dates or at different sites may still be compared meaningfully in
495 terms of PAD? Attenuation profiles were adjusted to a reference profile derived for each ROI from
496 the LMSQ780-2019 flight which covered both ROIs (Figure 1). Adjustment consisted in minimizing
497 the squared distance between profiles. Two different models were used to fit the targeted profiles
498 to the reference profile. The first one consisted in finding a single calibration coefficient, by fitting a
499 linear regression without intercept between profile values. The second model included an
500 intercept and an additional covariate, the mean distance to sensor of each vegetation layer. Note
501 that this covariate was highly correlated with height above ground at plot scale ($r > 0.99$).

502

503 Model 1

$$504 \quad \text{target}_i = \text{reference}_i \cdot \alpha + \varepsilon_i \quad \text{equation 4}$$

505 Model 2

$$506 \quad \text{target}_i = \text{reference}_i \cdot \alpha + \text{distance}_i \cdot \beta + \gamma + \varepsilon_i \quad \text{equation 5}$$

507 Where

508 i is an index referring to height (varies from 1 to 45 m above ground)

509 target_i is the observed attenuation value at height i of profile to be adjusted

510 reference_i is the reference profile attenuation value at height i

511 distance_i is the mean distance to laser of profile to be adjusted at height i

512 ε_i the error term to be minimized

513 A more complex model including mean canopy depth per layer as an additional predictor was also
514 tested but did not improve the fit significantly.

515

516 ROI1. ALS extinction profiles (variable flight height and variable transmitted power) are presented
517 in Figure 4. MiniVUX (multiple flight heights) extinction profiles are presented in Figure 5.

518 Corresponding adjustment statistics are reported in Table 8.

519 ROI2. VUX (various transmitted power) and miniVUX (single flight) are presented in Figure 6.

520 Corresponding adjustment statistics are reported in Table 9.

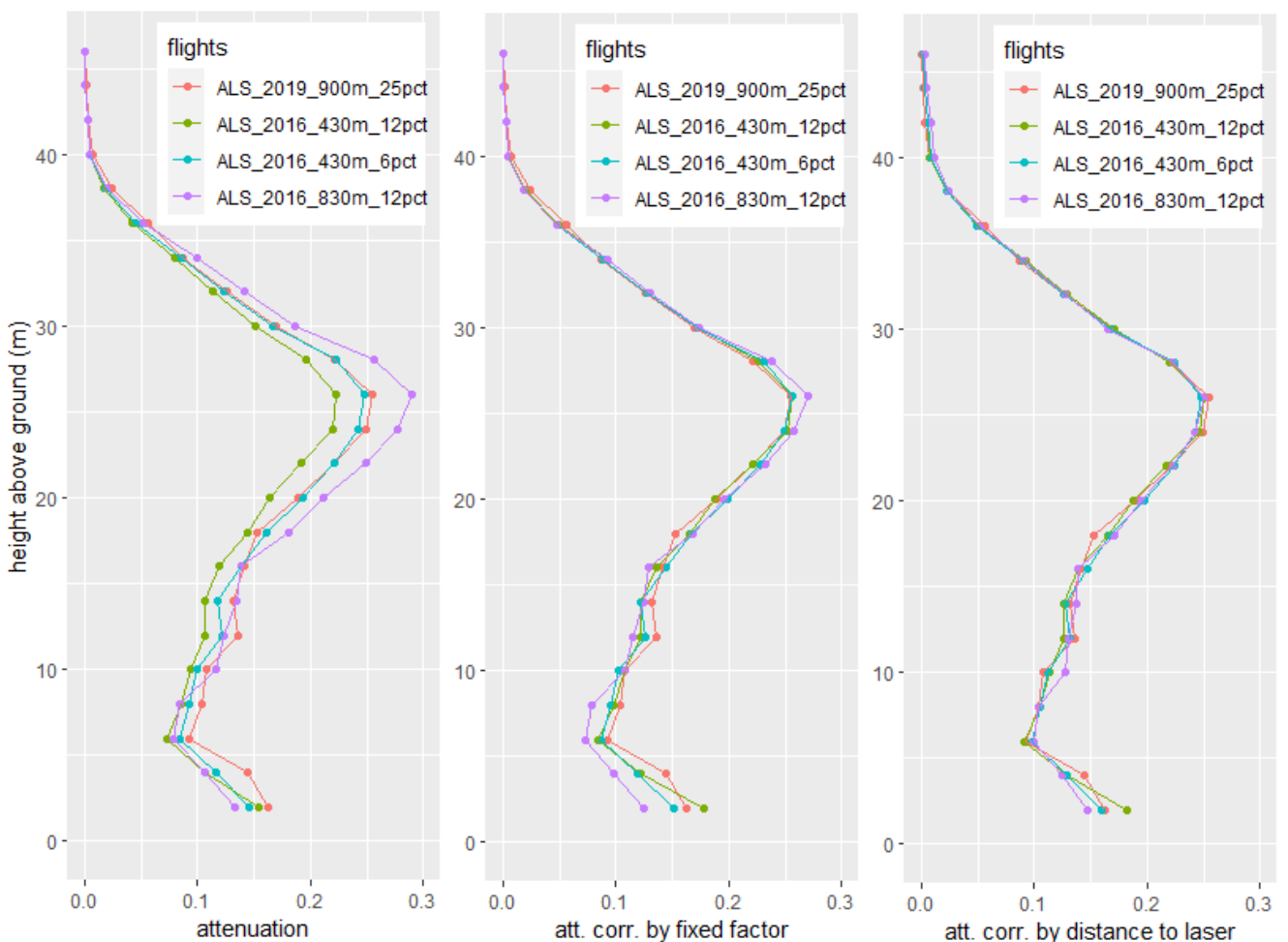


Figure 4: Inter calibration of ALS attenuation profiles obtained for different nominal flight heights (430m, 630m, 830m and 900m) and transmitted power (6%, 12% or 25% of full power). Left panel : raw profiles; center panel : profiles are adjusted to reference flight (900m 25%) by a simple constant correction coefficient; right panel : adjustment includes a linear effect of distance to laser.

Table 8: Attenuation profile adjustment statistics (ROI 1) - In bold lowest AIC and lowest residual standard error (rse) are highlighted showing improvement in fit when distance to laser is added as a predictor.

flight	rmse	rse_simple	calib. coef	rse_dist	AIC_simple	AIC_dist
ALS_430m_12pct	0.019	0.008	1.16	0.008	-203	-203
ALS_430m_6pct	0.009	0.007	1.05	0.005	-210	-224
ALS_830m_12pct	0.014	0.013	0.95	0.008	-172	-197
mnvx_low	0.019	0.011	0.89	0.007	-180	-205
mnvx_medium	0.028	0.011	0.83	0.008	-179	-200
mnvx_high	0.044	0.009	0.74	0.009	-197	-194

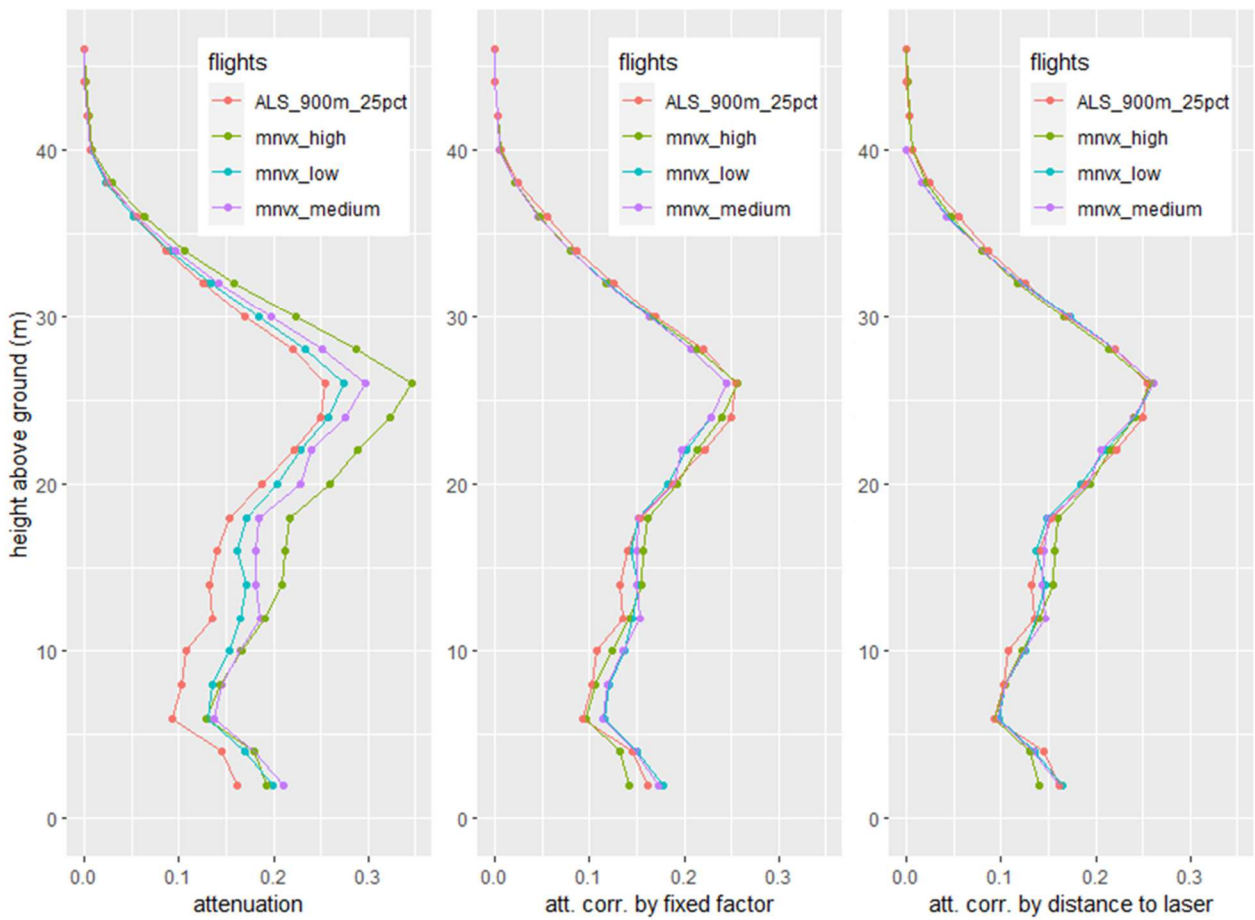
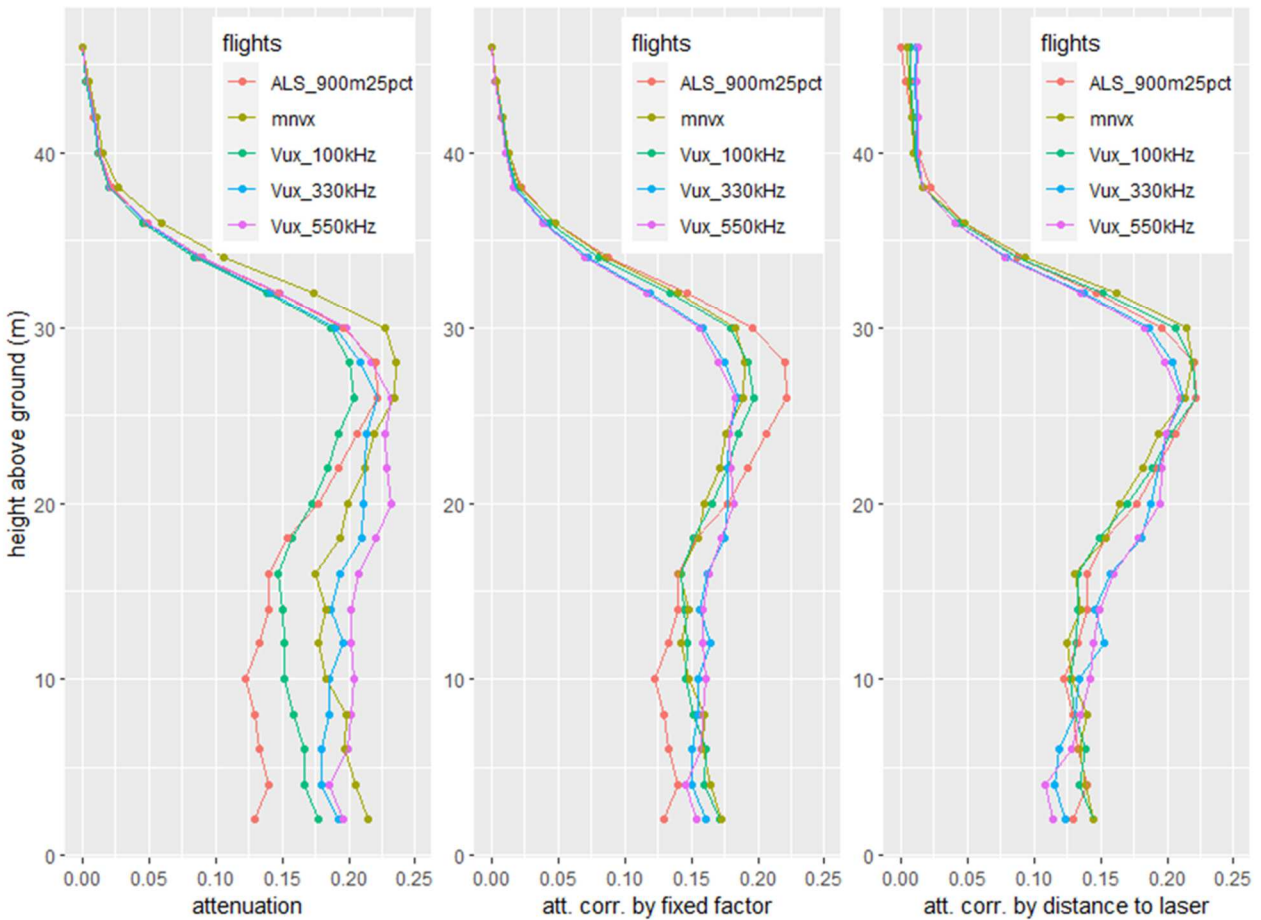


Figure 5: MiniVUX attenuation profiles obtained for different median flight heights above ground level (low = 58m, medium = 71m and high = 104m) plotted along ALS reference flight profile. Left panel: raw profiles; center panel: profiles are adjusted by means of a simple calibration coefficient ; right panel: calibration includes a linear effect of distance to laser.



521

Figure 6: VUX attenuation profiles obtained for different power settings, with miniVUX profile and with ALS reference profile. Left panel: raw profiles; center panel: profiles are adjusted by means of a simple calibration coefficient ; right panel: fitting incorporates a linear effect of distance to laser

522

Table 9: Attenuation profile adjustment statistics (ROI 2) of UAV lidar flights against reference ALS profile - In bold lowest AIC and lowest rse are highlighted showing improvement in fit when distance to laser is added as model predictor.

drone	rmse	rse_simple	Calib.coef	rse_dist	AIC_simple	AIC_dist
MiniVux	0.039	0.020	0.81	0.009	-112	-145
Vux_100kHz	0.018	0.018	0.96	0.006	-117	-163
Vux_330kHz	0.035	0.024	0.84	0.013	-104	-129
Vux_550kHz	0.044	0.025	0.79	0.015	-102	-123

523

524 Divergence between 2016-ALS profiles and reference 2019-ALS profile were globally smaller than the
525 divergence between UAV and 2019-ALS (Table 5 and Table 6). Lower at-canopy-irradiance flights had
526 profiles showing higher attenuation (e.g. ALS_830m_12%, Figure 4-left panel), higher at-canopy-irradiance
527 showed lower attenuation (e.g. ALS_430m_12%, Figure 4-left panel).

528 Divergence between UAV profiles and reference ALS profile increased with height of flight (miniVUX Table 5)
529 and with lower laser power (VUX Table 6).

530

531 The model including distance-to-laser as a covariate usually improved the fit (lower rse) compared to the
532 use of a simple calibration coefficient. The improvement was often very significant with a much lower AIC
533 (Table 5 and Table 6). Improvement in consistency between profiles is illustrated in Figure 4, Figure 5 and
534 Figure 6.

535 Residual error of VUX low power profiles (300kHz and 500kHz Pulse Repetition Rates) was larger than in any
536 other situation (see misfit in Figure 6 right panel).

537 Discussion

538 A general pattern was observed by which increasing at-canopy-irradiance led to higher penetration
539 and higher fragmentation rate. This was in line with previous studies which have reported similar
540 observations for other lidar sensors. Lee and Wang (2013) reported higher penetration rate
541 (proportion of ground point) at lower flying altitude over a subtropical forest, both with Optech
542 HD400 and Riegl LMS-Q680i. Næsset (2009) compared an Optech ALTM 1233 and an Optech ALTM
543 3100 operated at different flight heights and pulse repetition rates (PRR) over mature conifer
544 forest. That study reported a decrease in the proportion of multiple echoes with increasing flying
545 altitude and PRR. Such observations were made as part of a study exploring scanning settings

546 impact on digital terrain model quality (Lee and Wang 2013) or a study exploring scanning settings
547 impact on forest canopy metrics (Næsset 2009). They have not been interpreted in the context of
548 Plant Area Density estimation from lidar data and the implication of such observations in terms of
549 target under-detection do not seem to have not been fully recognized.

550 Part 1: individual return intensity analysis

551 This first analysis showed that apparent reflectance of vegetation targets was highly variable across tree
552 crowns (Figure 1) and that it also varied with canopy depth (Table 5). Both observations were true for the 3
553 sensors tested but responses varied according to sensor wavelength. While reflectance is expected to vary
554 with incident angle (see Equation 2 above), it is unlikely that spatial variation in leaf orientation might have
555 been the main driver of the observed patterns of change in apparent reflectance since the response varied
556 across sensors both in intensity and direction. The dependence of apparent reflectance on light incident
557 angle could be further investigated taking advantage of the large field of view of the miniVUX and VUX
558 sensors which were restricted to near-nadir incident angle in the present study (see Material and Methods
559 section). Dependence on canopy depth was particularly strong for the VUX operating at 1550nm. We also
560 found that a more complete retrieval of backscattered energy was achieved in case of higher at-canopy-
561 irradiance and in case of lower fragmentation rate.

562 Cumulative backscattered energy typically declined with increasing fragmentation (higher number of
563 returns per pulse). This may be a direct consequence of the intensity detection threshold as more
564 fragmented pulses are more likely to generate undetected returns. This may also indicate that a
565 higher pulse fragmentation decreases the detection rate. Successive hits by a downward travelling
566 pulse do not only gradually reduce its footprint but also its compactness (Figure S1). As a
567 consequence, detectability of small targets (relative to foot print size) will decrease and the
568 proportion of undetected interceptions (backscattered energy below the detection threshold) will

569 increase. This effect is expected to be dependent on the specific arrangement (size, density) of
570 scatterers and its contribution is difficult to evaluate and likely to vary across vegetation types.
571 Note that pulse compactness does not affect detectability of ground (non-porous target larger
572 than foot print size) which will depend on ground reflectivity and remaining transmitted power. In
573 some cases, we noted that higher fragmentation was associated with higher cumulative backscattered
574 energy (see for ex. 830m_12% flight in Figure 3A or 2B). The underlying logic for what may appear as
575 a paradox is in fact quite simple. The probability of detecting a target increases with target's
576 reflectivity. Therefore, a high number of returns is more likely to be observed if targets are more
577 reflective than average which also increases the cumulated energy per pulse. This pattern is
578 expected to be weaker or even absent under high at-canopy-irradiance since more complete
579 detection is less dependent on target reflectivity.

580

581 An increase in the at-canopy-irradiance was associated with a stronger drop in cumulative
582 backscattered energy of multiple returns shots (fig 3). Such a pattern may be explained as follows .
583 Pulses generating a single return may have been fully intercepted by a target larger than foot print
584 size or, alternatively, may correspond to an incompletely obstructed pulse (a "partial hit") which let
585 too little energy through (or a too highly fragmented pulse, see figure S1) for a second return to be
586 triggered further along the optical path. This might occur frequently given the porous structure of
587 the canopy. A typical echo is likely to be generated by interception of multiple scattered elements
588 of foliage which might allow some light to continue travelling undetected down the optical path.
589 Increasing the irradiance will increase the detection rate of secondary targets and thereby reduce
590 the frequency of single returns corresponding to only partially intercepted pulses by a single

591 target. As a result, the mean intensity of single returns (relative to the mean cumulated intensity of
592 multiple returns) increases when at-canopy-irradiance increases.

593

594 We have no clear explanation for the fact mean single return intensity did not increase with increased at-
595 canopy-irradiance for the miniVUX. This may be may be related to the change in size or shape of the
596 footprint with distance. A lower flight height determines a smaller pulse footprint at the top of the
597 canopy and hence a deeper penetration of pulse prior to triggering a return. The mean single
598 return height was only slightly affected: respectively equal to 27.56, 27.40 and 27.26m for the 3
599 flight heights. This will nonetheless have affected mean irradiance of target and target reflectivity.

600 A General Additive Model of intensity as a function of canopy depth (not presented) showed a
601 non-linear trend of single return intensity with canopy depth in the upper canopy which might
602 have compensated the expected increase in intensity.

603

604 High variability in target reflectivity made individual return intensity an unreliable proxy of the fraction of
605 pulse intercepted per hit. Instead, we estimated the contribution of each return by the mean return
606 intensity per return rank per return number (after excluding any shot reaching the ground).

607

608 In a previous study (Vincent et al. 2017) conducted with a different sensor (Riegl LMSQ560, 1550nm), the
609 mean cumulative returned intensity per emitted pulse was reported to be independent of the number of
610 returns per pulse. This was taken as an argument that undetected backscattered energy would either be
611 small or independent of the degree of fragmentation. Hence the average intensity (over all returns of
612 identical relative rank) was taken as an estimate of the contribution of a return to pulse interception. In
613 other words, averaging out the high variability of target reflectivity, the mean relative intensity per return

614 rank per number of returns, was expected to provide the best estimate of individual return contribution to
615 laser pulse interception.

616 A more thorough examination of patterns of return intensity which was permitted by the comparison across
617 sensors and settings revealed that loss of returned energy was not generally negligible.

618

619 It was found for two sensors that fragmentation reduced the cumulative retrieved energy (with losses of c.
620 10%-20% Figure 3A & B). The third sensor (VUX) which operated at the same wavelength as the sensor used
621 in the 2017 study, showed no reduction in cumulative intensity with fragmentation, but rather the opposite
622 pattern (Figure 3C and D). This pattern largely disappeared however once the dependency of return
623 intensity on canopy depth was corrected for. The apparently stable cumulative return intensity observed
624 probably reflected an imperfect correction of the dependency of individual return intensity on canopy
625 depth which was based on single returns. Not only was the correction model applied fairly crude but also
626 single returns further away from the top of the canopy were more likely to be incomplete (partially
627 intercepted without detectable additional return) than returns occurring higher up in the canopy. This might
628 have introduced a negative bias in the correction model.

629 The correction of this systematic variation in target reflectivity with canopy depth aimed at limiting the
630 distortion between reflected energy and area of intercepting surface. However, it did not correct for
631 detection bias.

632

633 The LMSQ780 2019 data which covered both ROIs showed a low level of dependence of intensity on canopy
634 depth (Table 5) and a balanced ground to vegetation intensity (Table 7). We selected that dataset to develop
635 a single statistical model of contribution of successive returns to laser pulse interception. Weights were first
636 computed per ROI and were found to be very consistent across ROIs (Appendix 3). We then applied the
637 same single matrix of individual return weights to all flights to compute light attenuation in AMAPVox.

638

639 Part 2 : intercalibration of extinction profiles

640 In this study we focused on two small ROIs (1.4 ha and 2 ha respectively) which did not capture the
641 horizontal and vertical variability in vegetation structure found at the site level (10km²). Detection
642 bias is expected to vary with vegetation structure and show some variability both within and across
643 sites (under constant acquisition settings). Previous work (Shao et al. 2019) suggests however that
644 single intercalibration functions/coefficients may hold at site level, at least in first approximation.

645

646 **Divergence of profiles (prior to intercalibration)**

647 A systematic pattern of higher apparent extinction coefficient under lower at-canopy-irradiance (left most
648 panel of Figure 4, Figure 5 and Figure 6) was found.

649 For a given system when the top of canopy irradiance increased (due to higher transmitted power, or lower
650 flight height) the proportion of pulses reaching the ground (a measure of laser penetration) increased, i.e.
651 ground detection rate increased (Table 1 & Table 2). Detection rate of the most distant targets was
652 enhanced. While higher irradiance may, in principle, also improve detection of small close-by targets, the
653 major impact was an increase in the detection of more distant targets.

654 The larger beam divergence of the miniVUX was responsible for a more rapid decrease in irradiance with
655 increasing distance to laser. In addition, the received power is proportional to the inverse of the squared
656 distance from laser to target (*Equation 2*). For a low flying altitude DLS, this distance varies by a factor of 2
657 and the power decreases by a factor 4 from top to bottom of canopy. Hence, detection rate by the miniVUX
658 was expected to decrease significantly from top to bottom of canopy (Figure 4a). In fact, including this
659 distance dependent correction proved critical for reducing residual standard error (Table 8) when flight
660 height was lowest (and relative change in irradiance per unit distance was largest).

661

662 **Effectiveness of intercalibration**

663 Overall, calibration by a constant coefficient reduced the inter-profile residual standard error by a
664 factor of ~ 2 while including distance to laser reduced the error by a factor of ~ 3 (Table 8 & Table 9).
665 The level of initial discrepancy and the level of reduction in error was however highly variable
666 across flights. The poorest fit (RMSE > 0.01 , \sim relative RMSE $> 10\%$) occurred for VUX operated at
667 low power (330kHz and 550kHz).

668

669 **Source of residual misfit**

670 The different detectability of ground, wood and leaves at 1550nm (Table 6. and (Brede et al. 2022))
671 was probably responsible for a complex distortion pattern of the profile at low power setting which
672 prevented a simple model to effectively correct for this bias. At high power the level of under
673 detection seemed to be limited though and a correction using distance to laser as covariate
674 effectively aligned the VUX 100kHz profile to the reference ALS profile.

675

676 **Absolute calibration**

677 We selected the LMSQ780-25% power 2019 ALS flight covering both ROIs as the reference flight to
678 which the attenuation profiles were fitted. However, comparison with lower altitude flights and
679 higher at-canopy irradiance flights conducted with the same sensor on ROI1 (e.g. ALS_430m_12%)
680 indicated that this attenuation reference profile was probably positively biased (by at least 16%,
681 see Table 8). The same conclusion (likely positive attenuation bias) can be drawn from the
682 comparison of the number of shots triggering a ground echo (7.3% for ALS_430m_12% - Table 2 -
683 against 5.2% for ALS_900m_25% reference flight - Table 3).

684 A method for absolute calibration would be desirable as a reference flight will not usually be
685 available across campaigns. This could be attempted by simulating light transfer in the voxelized
686 scene and comparing light transmittance maps with measurement taken in situ (Vincent et al.
687 2017). However, given the high variation in time-integrated light intensity which is known to occur
688 over short distances in the forest understory (Baraloto and Coueron 2010; Vincent et al. 2017), a
689 dense ground sampling pattern would then be required, and any ground reference measurements
690 would need to be accurately geo-positioned to be compared with the ALS data.

691 Another strategy would be to use terrestrial laser scanning to derive reference extinction
692 coefficients for sample plots. Some terrestrial lasers have ranges in excess of 500m. Hence, they
693 are unlikely to suffer from significant under-detection of vegetation below 50m range. There is
694 however a difference in acquisition geometry due to sensors position. In TLS, the vegetation layers
695 close to the ground are mostly sampled by pulses emitted at inclination angles close to the
696 horizontal whereas the upper canopy layers are predominantly sampled with an angle close to the
697 vertical. In case of strong anisotropy in light extinction, direct adjustment of attenuation profile
698 derived with one sensor to the attenuation profile derived with the other may not yield valid
699 results. In addition, absolute calibration of TLS derived attenuation rates would still be required
700 noting that TLS systems also vary in wavelength, pulse duration and recording capabilities.

701 The most straightforward strategy would probably be to fly again over part of the scanned area at
702 much higher at-canopy-irradiance, assuming that the under-detection bias would then be
703 negligible. Comparing detection rate for gradually decreasing power may provide a way to check
704 that detection rate reaches acceptable levels at maximum power. Modern lidar systems such as
705 the LMSQ780 are designed for mapping large areas and are able to operate at high altitude (up to

706 4700m for the LMSQ780 according to the manufacturer's technical data sheet (RIEGL Laser
707 Measurement Systems 2015). Flying at 900m (the cruising altitude of our reference flight) the at-
708 canopy-irradiance could in principle be increased by a factor of 16 by increasing nominal power
709 from 25% to 100% and decreasing PRR from 400KHz to 100KHz. At-canopy-irradiance could be
710 increased further by flying lower if necessary. Hence there is a considerable margin to improve
711 completeness of target detection without risking ocular hazard (Nominal Ocular Hazard Distance is
712 given at 200m for the LMSQ780 lidar operated at full power 100kHz PRR) thereby achieving a
713 robust estimate of the true detection bias affecting lidar data collected under standard settings.

714 Conclusion

715 We found that a more complete retrieval of backscattered energy was achieved in the case of
716 higher at-canopy-irradiance. Incomplete target detection generated a positive bias in light
717 attenuation coefficient and consequently in PAD. Positive bias was due to the fact that more
718 distant targets were less consistently detected. In a series of hits along an optical path, foremost
719 interceptions will tend to be larger as pulse effective footprint is larger. Therefore, foremost targets
720 are more systematically detected. The general pattern can be modulated by differential reflectivity
721 of ground and vegetation or of different vegetation elements.

722

723 Systematic increase of reflectivity with canopy depth observed at 1550nm had not been noted in a
724 previous study conducted on the same site with another sensor operating at the same wavelength
725 (Vincent et al. 2017). This variation in vegetation reflectivity probably masked a decrease in
726 detection rate with fragmentation and led the authors to the wrong conclusion that detection bias
727 was negligible.

728

729 Biases in light attenuation related to incomplete target detection may be large. Considering for
730 instance the highest at-canopy irradiance experimented in the present study (ALS-430m 12%
731 power) as the reference, it was observed that ALS attenuation profiles were typically
732 overestimated by 15 to 20% and UAV by 20 to 25%. This means that PAD will also be overestimated
733 in the same proportion. These are lower bound estimates of detection bias. True bias could be
734 approached using as a reference a saturating at-canopy-irradiance (showing no increase in
735 detection rate with further increase in at-canopy-irradiance).

736

737 Intercalibration of lidar overflights conducted with the LMSQ780 or miniVUX at different altitude
738 or power settings was satisfactory. Sensors operating at wavelengths more different from each
739 other were more difficult to intercalibrate and simple methods like those presented here were not
740 totally effective. They notably failed to properly align low power VUX flights with the rest of the
741 flights. A fine calibration between sensors operating at different wavelength would probably
742 require reformulating the model which describes pulse interception by vegetation elements at
743 voxel level by including an estimate of censorship. Predicting the likelihood of local under-
744 detection may be possible but is not straightforward because target detectability will not only
745 depend on effective footprint size and distance to laser as shown here, but also on unknown
746 features such as optical properties, spatial arrangement and size of vegetation elements. TLS data
747 which can give access to leaf-wood segmentation and, at least at close range, to the orientation of
748 vegetation elements (Bailey and Mahaffee 2017; Vicari et al. 2019; Stovall et al. 2021) may provide
749 an opportunity to integrate local correction for detection rate. However, transferability to

750 landscape scale ALS data would remain an issue. The use of simulated data (Yin et al. 2020) may
751 offer another avenue to model censorship based on the statistical analysis of the point cloud
752 geometric and radiometric features.

753

754 *Acknowledgements*

755 This is a publication of Laboratoire d'Excellence CEBA (ANR-10-LABX-25). This study benefited from
756 funding by the Centre National d'Etudes Spatiales [grant n°4500063412 and 4500066841 – Tosca
757 BIOMASS], and the European Spatial Agency [ESA AO/1-9584/18/NL/AI FORESTSCAN]

758

759 *Description of author's responsibilities.*

760 Conceptualization, Writing - Original Draft GV; Methodology GV, PV, NB, BB; data collection NB, BB,
761 GV, JB, IC; formal analysis GV, EM, GD; Software PV; Writing - Review & Editing ALL.

762 References

- 763 Almeida DRA de, Stark SC, Shao G, Schietti J, Nelson BW, Silva CA, Gorgens EB, Valbuena R, Papa D
764 de A, Brancalion PHS (2019) Optimizing the Remote Detection of Tropical Rainforest
765 Structure with Airborne Lidar: Leaf Area Profile Sensitivity to Pulse Density and Spatial
766 Sampling. *Remote Sensing* 11:92. <https://doi.org/10.3390/rs11010092>
- 767 Arnqvist J, Freier J, Dellwik E (2020) Robust processing of airborne laser scans to plant area density
768 profiles. *Biogeosciences* 17:5939–5952. <https://doi.org/10.5194/bg-17-5939-2020>
- 769 Bailey BN, Mahaffee WF (2017) Rapid measurement of the three-dimensional distribution of leaf
770 orientation and the leaf angle probability density function using terrestrial LiDAR scanning.
771 *Remote Sensing of Environment* 194:63–76. <https://doi.org/10.1016/j.rse.2017.03.011>
- 772 Baraloto C, Couteron P (2010) Fine-scale Microhabitat Heterogeneity in a French Guianan Forest.
773 *Biotropica* 42:420–428. <https://doi.org/10.1111/j.1744-7429.2009.00620.x>
- 774 Bonan G (ed) (2015) *Plant Canopies*. In: *Ecological Climatology: Concepts and Applications*, 3rd
775 edn. Cambridge University Press, Cambridge, pp 264–288
- 776 Bréda NJJ (2003) Ground-based measurements of leaf area index: a review of methods,
777 instruments and current controversies. *J Exp Bot* 54:2403–2417
- 778 Brede B, Bartholomeus HM, Barbier N, Pimont F, Vincent G, Herold M (2022) Peering through the
779 thicket: Effects of UAV LiDAR scanner settings and flight planning on canopy volume
780 discovery. *International Journal of Applied Earth Observation and Geoinformation*
781 114:103056. <https://doi.org/10.1016/j.jag.2022.103056>

782 Chen JM, Black TA (1991) Measuring leaf area index of plant canopies with branch architecture.
783 Agricultural and Forest Meteorology 57:1–12. <https://doi.org/10.1016/0168->
784 1923(91)90074-Z

785 Chen JM, Rich PM, Gower ST, Norman JM, Plummer S (1997) Leaf area index of boreal forests:
786 Theory, techniques, and measurements. J Geophys Res 102:29429–29443.
787 <https://doi.org/10.1029/97JD01107>

788 Fang H, Baret F, Plummer S, Schaepman-Strub G (2019) An Overview of Global Leaf Area Index
789 (LAI): Methods, Products, Validation, and Applications. Reviews of Geophysics 57:739–799.
790 <https://doi.org/10.1029/2018RG000608>

791 Frost C, Thompson SG (2000) Correcting for Regression Dilution Bias: Comparison of Methods for a
792 Single Predictor Variable. Journal of the Royal Statistical Society Series A (Statistics in
793 Society) 163:173–189

794 Höfle B, Pfeifer N (2007) Correction of laser scanning intensity data: Data and model-driven
795 approaches. ISPRS Journal of Photogrammetry and Remote Sensing 62:415–433.
796 <https://doi.org/10.1016/j.isprsjprs.2007.05.008>

797 Hopkinson C, Chasmer LE (2007) Modeling canopy gap fraction from lidar intensity. In: IAPRS
798 Volume XXXVI. Espoo, Finland, p Part 3 / W52

799 Kaasalainen S, Hyyppä H, Kukko A, Litkey P, Ahokas E, Hyyppä J, Lehner H, Jaakkola A, Suomalainen
800 J, Akujarvi A, Kaasalainen M, Pyysalo U (2009) Radiometric Calibration of LIDAR Intensity

801 With Commercially Available Reference Targets. IEEE Transactions on Geoscience and
802 Remote Sensing 47:588–598. <https://doi.org/10.1109/TGRS.2008.2003351>

803 Laurans M, Martin O, Nicolini E, Vincent G (2012) Functional traits and their plasticity predict
804 tropical trees regeneration niche even among species with intermediate light requirements.
805 Journal of Ecology 100:1440–1452. <https://doi.org/10.1111/j.1365-2745.2012.02007.x>

806 Lee C-C, Wang C-K (2013) LiDAR Penetration Comparison at Different Altitudes and Scanning
807 Angles in Subtropical Forest

808 Longo M, Saatchi S, Keller M, Bowman K, Ferraz A, Moorcroft PR, Morton DC, Bonal D, Brando P,
809 Burbank B, Derroire G, dos-Santos MN, Meyer V, Saleska S, Trumbore S, Vincent G (2020)
810 Impacts of Degradation on Water, Energy, and Carbon Cycling of the Amazon Tropical
811 Forests. Journal of Geophysical Research: Biogeosciences n/a:e2020JG005677.
812 <https://doi.org/10.1029/2020JG005677>

813 Miller J (1967) A formula for average foliage density. Australian Journal of Botany 15:141–144.
814 <https://doi.org/10.1071/BT9670141>

815 Morsdorf F, Kötz B, Meier E, Itten KI, Allgöwer B (2006) Estimation of LAI and fractional cover from
816 small footprint airborne laser scanning data based on gap fraction. Remote Sensing of
817 Environment 104:50–61

818 Næsset E (2009) Effects of different sensors, flying altitudes, and pulse repetition frequencies on
819 forest canopy metrics and biophysical stand properties derived from small-footprint

820 airborne laser data. *Remote Sensing of Environment* 113:148–159.
821 <https://doi.org/10.1016/j.rse.2008.09.001>

822 Olivas PC, Oberbauer SF, Clark DB, Clark DA, Ryan MG, O’Brien JJ, Ordoñez H (2013) Comparison of
823 direct and indirect methods for assessing leaf area index across a tropical rain forest
824 landscape. *Agricultural and Forest Meteorology* 177:110–116.
825 <https://doi.org/10.1016/j.agrformet.2013.04.010>

826 Osada N, Takeda H, Furukawa A, Awang M (2001) Leaf dynamics and maintenance of tree crowns
827 in a Malaysian rain forest stand. *Journal of Ecology* 89:774–782

828 R Core Team. (2022) R: A language and environment for statistical computing

829 Reich PB, Uhl C, Walters MB, Prugh L, Ellsworth DS (2004) Leaf demography and phenology in
830 Amazonian rain forest: A census of 40 000 leaves of 23 tree species. *Ecological Monographs*
831 74:3–23

832 Riegl Laser Measurement Systems (2019) LAS extrabytes implementation in RIEGL software -
833 WHITEPAPER. Riegl Laser Measurement Systems GmbH

834 RIEGL Laser Measurement Systems (2020) RIEGL VUX-1UAV Datasheet

835 RIEGL Laser Measurement Systems (2015) RIEGL LMS-Q780 Datasheet

836 RIEGL Laser Measurement Systems (2022) RiParameter

837 Ross J (1981) *The radiation regime and architecture of plant stands*. Springer Netherlands

838 Shabanov NV, Huang D, Yang W, Tan B, Knyazikhin Y, Myneni RB, Ahl DE, Gower ST, Huete AR,
839 Aragao LEOC, Shimabukuro YE (2005) Analysis and optimization of the MODIS leaf area
840 index algorithm retrievals over broadleaf forests. *IEEE Transactions on Geoscience and*
841 *Remote Sensing* 43:1855–1865. <https://doi.org/10.1109/TGRS.2005.852477>

842 Shao G, Stark SC, de Almeida DRA, Smith MN (2019) Towards high throughput assessment of
843 canopy dynamics: The estimation of leaf area structure in Amazonian forests with
844 multitemporal multi-sensor airborne lidar. *Remote Sensing of Environment* 221:1–13.
845 <https://doi.org/10.1016/j.rse.2018.10.035>

846 Solberg S, Brunner A, Hanssen KH, Lange H, Næsset E, Rautiainen M, Stenberg P (2009) Mapping
847 LAI in a Norway spruce forest using airborne laser scanning. *Remote Sensing of*
848 *Environment* 113:2317–2327. <https://doi.org/10.1016/j.rse.2009.06.010>

849 Stovall AEL, Masters B, Fatoyinbo L, Yang X (2021) TLSLeAF: automatic leaf angle estimates from
850 single-scan terrestrial laser scanning. *New Phytologist* 232:1876–1892.
851 <https://doi.org/10.1111/nph.17548>

852 Vicari MB, Pisek J, Disney M (2019) New estimates of leaf angle distribution from terrestrial LiDAR:
853 Comparison with measured and modelled estimates from nine broadleaf tree species.
854 *Agricultural and Forest Meteorology* 264:322–333.
855 <https://doi.org/10.1016/j.agrformet.2018.10.021>

856 Vincent G, Antin C, Laurans M, Heurtebize J, Durrieu S, Lavalley C, Dauzat J (2017) Mapping plant
857 area index of tropical evergreen forest by airborne laser scanning. A cross-validation study

858 using LAI2200 optical sensor. *Remote Sensing of Environment* 198:254–266.
859 <https://doi.org/10.1016/j.rse.2017.05.034>

860 Vincent G, Pimont F, Verley P (2021) A note on PAD/LAD estimators implemented in AMAPVox 1.8

861 Vincent G, Sabatier D, Blanc L, Chave J, Weissenbacher E, Pélissier R, Fonty E, Molino JF, Couteron P
862 (2012) Accuracy of small footprint airborne LiDAR in its predictions of tropical moist forest
863 stand structure. *Remote Sensing of Environment* 125:23–33.
864 <https://doi.org/10.1016/j.rse.2012.06.019>

865 Vincent G, Weissenbacher E, Sabatier D, Blanc L, Proisy C, Couteron P (2010) Détection des
866 variations de structure de peuplements en forêt dense tropicale humide par Lidar
867 aéroporté (Small foot-print airborne LiDAR proves highly sensitive to changes in structure of
868 moist tropical forest). *Revue Française de Photogrammétrie et Télédétection* 191:42–50

869 Wagner W (2010) Radiometric calibration of small-footprint full-waveform airborne laser scanner
870 measurements: Basic physical concepts. *ISPRS Journal of Photogrammetry and Remote*
871 *Sensing* 65:505–513. <https://doi.org/10.1016/j.isprsjprs.2010.06.007>

872 WeiChen H, Shih TianYuan [Shih TYP, HungCheng C, JinKing L (2015) A study on factors affecting
873 airborne LiDAR penetration. *TAO - Terrestrial, Atmospheric and Oceanic Sciences* 26:241–
874 251

875 Wojtanowski J, Zygmunt M, Kaszczuk M, Mierczyk Z, Muzal M (2014) Comparison of 905 nm and
876 1550 nm semiconductor laser rangefinders' performance deterioration due to adverse

877 environmental conditions. *Opto-Electron Rev* 22:183–190. [https://doi.org/10.2478/s11772-](https://doi.org/10.2478/s11772-014-0190-2)
878 014-0190-2

879 Yin T, Qi J, Cook BD, Morton DC, Wei S, Gastellu-Etchegorry J-P (2020) Modeling Small-Footprint
880 Airborne Lidar-Derived Estimates of Gap Probability and Leaf Area Index. *Remote Sensing*
881 12:4. <https://doi.org/10.3390/rs12010004>

882 Zheng G, Moskal LM (2009) Retrieving Leaf Area Index (LAI) Using Remote Sensing: Theories,
883 Methods and Sensors. *Sensors* 9:2719–2745. <https://doi.org/10.3390/s90402719>

884